

Ekman Pumping and the Energetics of the Southern Hemisphere Eddy Life Cycle

CORY BAGGETT

Department of Meteorology, The Pennsylvania State University, University Park, Pennsylvania

SUKYOUNG LEE

Department of Meteorology, The Pennsylvania State University, University Park, Pennsylvania, and Seoul National University, Seoul, South Korea

(Manuscript received 5 September 2013, in final form 25 March 2014)

ABSTRACT

In the framework of the Lorenz energy cycle, the climatological and eddy life cycle characteristics of the generation of eddy available potential energy through Ekman pumping (EEPE) are evaluated using Interim European Centre for Medium-Range Weather Forecasts (ECMWF) Re-Analysis (ERA-Interim) data (1979–2011). EEPE exhibits an annual cycle that is maximized during a given hemisphere's winter, with maximum values in the midtroposphere of the midlatitudes.

Spectral analysis of the Southern Hemisphere storm track reveals that positive EEPE is associated with an anomalously small vertical phase tilt. A composite analysis of the Southern Hemisphere eddy life cycle reveals a maximum in EEPE that occurs after the peak eddy amplitude. Eddy life cycles during winter with large values of EEPE have higher values of eddy available potential energy and eddy kinetic energy than life cycles with small EEPE. However, baroclinic energy conversion remains unenhanced in life cycles with large values of EEPE. The lack of enhancement of baroclinic conversion is related to the small vertical phase tilt associated with positive EEPE. Instead, barotropic energy conversion is muted, and it is this muted barotropic decay that results in an amplification of eddy kinetic energy. There is no evidence of reflecting critical latitudes playing a role in this reduction of barotropic decay, as found in previous modeling studies. Rather, during Southern Hemisphere winter, this reduction coincides with the presence of a turning latitude on the equatorward side of the storm track.

1. Introduction

Atmospheric eddies play a crucial role in the redistribution of Earth's energy and moisture. Over large portions of Earth's surface, particularly in the midlatitudes, eddies are the primary drivers of sensible weather in the form of synoptic-scale storm systems. One mechanism that affects eddies is surface friction. The direct effect of surface friction is to dampen eddy energy. However, surface friction may indirectly cause eddy amplitudes to grow by reducing the horizontal shear of the background zonal wind (James and Gray 1986; James 1987). More recently, in the context of subcritical instability in a two-layer quasigeostrophic (QG) model (Lee and Held 1991), Lee (2010b) found

that in the model's parameter space where total eddy energy increases with enhanced Ekman friction, Ekman pumping energizes eddies by directly enhancing eddy available potential energy. This process is also accompanied by a reduction of the barotropic decay of the eddies (Lee 2010a). In fact, Lee and Held (1991) and Lachmy and Harnik (2009) attributed their finite-amplitude eddy solution to this muted barotropic decay. The influence of Ekman pumping and muted barotropic decay on eddies, as identified by the QG model, will be addressed in this study using a global reanalysis dataset.

Our analysis will follow the conceptual framework of the Lorenz energy cycle (Lorenz 1955). Lorenz stated that energy flows from zonal available potential energy P_M , to eddy available potential energy P_E , to eddy kinetic energy K_E , and finally to zonal kinetic energy K_M . Depending on the vertical phase tilt between the eddies in the upper and lower levels of the atmosphere, vertical motions induced by Ekman pumping may produce either K_E or P_E . If the vertical phase difference between

Corresponding author address: Cory Baggett, Department of Meteorology, The Pennsylvania State University, 503 Walker Building, University Park, PA 16802.
E-mail: cfb128@psu.edu

the lower and upper waves is less (greater) than $1/4$ wavelength, then Ekman pumping enhances the conversion from K_E to P_E (from P_E to K_E). In sum, the direct effect of surface friction is to damp the total eddy energy. However, the vertical motions induced by Ekman pumping may cause either P_E or K_E to increase individually. If Ekman pumping is generating P_E (and thereby enhancing the variance of temperature), then it is shown by Lee (2010b) that there is an enhancement of baroclinic conversion from P_M to P_E . This indirect effect of enhanced baroclinic conversion allows the eddies to gain energy beyond what is lost in the direct effect to frictional dissipation. Because friction acts to energize the eddies, this process is referred to as dissipative energization (Lee 2010b).

Using reanalysis data, the following questions are addressed in this study. First, from the perspective of the Lorenz energy cycle, what are the climatological values of eddy conversion due to Ekman pumping? Second, in the Southern Hemisphere (SH) is the generation of P_E (K_E) through Ekman pumping observed when the waves in the upper and lower levels of the atmosphere are more (less) in phase? Third, is enhanced baroclinic conversion (dissipative energization) observed when Ekman pumping is generating P_E or is reduced barotropic decay and enhanced K_E observed? Finally, what physical explanations may be applied to the results of the previous questions? It should be noted that the results of this study are observational in nature with the aim of quantifying atmospheric properties and eddy life cycle characteristics in the presence of Ekman pumping that is generating either K_E or P_E . There is no intention to imply a cause-and-effect relationship between the observed results and Ekman pumping.

The focus of this paper is primarily the SH. The SH has a mostly uniform surface that allows the study of Ekman pumping with relatively smaller effects from large-scale topography and stationary waves. Furthermore, the SH is shown by this study to have a larger predisposition to generate P_E by Ekman pumping than the Northern Hemisphere (NH), which allows the results of Lee (2010b) to be tested using reanalysis data.

2. Data and methods

a. Data

All of the variables required to compute the energetics and eddy available potential energy through Ekman pumping (EEPE) derive from the Interim European Centre for Medium-Range Weather Forecasting (ECMWF) Re-Analysis (ERA-Interim) project (Dee et al. 2011). ERA-Interim data are currently available

on a global fixed grid with a horizontal resolution of $0.75^\circ \times 0.75^\circ$, a vertical resolution of 37 pressure levels, and four time steps per day. We interpolate most data to a resolution of $2.5^\circ \times 2.5^\circ$ and 23 pressure levels, while only using the 0000 UTC time step. By broadening the resolution, the computational time of the calculations is reduced, while not diminishing the larger-scale global and synoptic features that are desired. However, for our calculation of EEPE, we acquire additional geopotential and temperature data at a vertical resolution of 25 hPa in the boundary layer.

For this study, the following variables are obtained from ERA-Interim: zonal wind u , meridional wind v , vertical velocity ω (Pa s^{-1}), temperature T , geopotential Z , 2-m temperature T_{2m} , surface pressure p_{SFC} , boundary layer height z_{BL} , instantaneous zonal surface stress τ_x , and instantaneous meridional surface stress τ_y . Each of these variables is a function of time, latitude, and longitude, while u , v , ω , T , and Z have an additional dimension in the vertical. All of the variables are derived from observations with the exception of z_{BL} , τ_x , and τ_y . These variables are 12-h forecast variables, so they derive from the prior 1200 UTC reanalysis. The scope of this study extends from 1979 to 2011.

b. Calculation of the vertical profile of the Ekman pumping vertical velocity

The Ekman pumping vertical velocity at the top of the boundary layer is calculated daily at every grid point following Mason and Sykes (1978), such that

$$\omega_{\text{Ek}} = -\frac{g}{f} \left(\frac{\partial \tau_y}{\partial x} - \frac{\partial \tau_x}{\partial y} \right),$$

where the synoptic-scale approximation of $\omega_{\text{Ek}} = -\rho g w_{\text{Ek}}$ has been employed, $f = 2\Omega \sin \varphi$ is the Coriolis parameter, φ is latitude, Ω is Earth's angular velocity, g is the acceleration of gravity, w is vertical velocity (m s^{-1}), and ρ is density. Having calculated ω_{Ek} at the top of the boundary layer, it is now necessary to construct a vertical profile of ω_{Ek} throughout the entire depth of the troposphere at reanalysis pressure levels both above and below the pressure level of the boundary layer p_{BL} . We estimate p_{BL} from z_{BL} using the geopotential height of reanalysis pressure levels. Since z_{BL} has units of meters above the terrain, z_{BL} is added to the height of the terrain z_{TERR} . We then locate the two reanalysis pressure levels whose geopotential height lies on each side of $z_{\text{BL}} + z_{\text{TERR}}$ and linearly interpolate to find p_{BL} . It is worth mentioning that the accuracy of our estimation of p_{BL} is dependent on the accuracy of z_{BL} as provided by ERA-Interim. Köhler et al. (2011) found there is a bias of underestimating the height of the boundary layer by

approximately 100–200 m in marine environments. This bias is likely introduced into our results due to our focus on the SH.

The vertical profile of ω_{Ek} is now constructed at all reanalysis pressure levels. In the boundary layer, we let ω_{Ek} increase linearly from zero at p_{SFC} to its maximum magnitude at p_{BL} according to

$$\omega_{\text{Ek}}|_p = \omega_{\text{Ek}}|_{p_{\text{BL}}} \left(\frac{p_{\text{SFC}} - p}{p_{\text{SFC}} - p_{\text{BL}}} \right). \quad (1)$$

Above p_{BL} , we let ω_{Ek} decrease exponentially by applying the theoretical framework of the rotating tank experiments of Holton (1965) to the real atmosphere, such that

$$\omega_{\text{Ek}}|_p = \omega_{\text{Ek}}|_{p_{\text{BL}}} \exp[-(z - z_{\text{BL}} - z_{\text{TERR}})/D], \quad (2)$$

where z is the geopotential height of a reanalysis pressure level and D is the scale height. According to Eq. (14) of Holton (1965), the height D can be scaled as

$$D = H\sqrt{\varepsilon} = \sqrt{\frac{f^2 L^2 H}{g(\Delta\theta/\theta_{\text{SFC}})}}, \quad (3)$$

where L and H are the radius and depth of the tank, respectively, and $\Delta\theta$ is the potential temperature difference between the tropopause and the surface. To apply this result to the atmosphere, we regard H as being the difference between the height of the tropopause and the height of the terrain, and we set L equal to one-fourth the length of zonal wavenumber 6. We test other zonal wavenumbers in our results section for sensitivity. The parameter ε is the dimensionless, internal rotational Froude number, the ratio of the forces due to rotation and buoyancy (Holton 1965). In our definition of ε , we have substituted $\Delta\theta/\theta_{\text{SFC}}$ in place of $\Delta\rho/\rho_{\text{SFC}}$ because the atmosphere is a compressible fluid. Finally, at all reanalysis pressure levels above the tropopause p_{TROP} , we set $\omega_{\text{Ek}} = 0$. Although this produces a delta function in divergence of ω_{Ek} at the tropopause, we assume that the enhanced stability found at the tropopause will suppress any vertical motions due to Ekman pumping. For zonal wavenumber 6, we found that D is typically about 5–10 km, implying that at the tropopause, ω_{Ek} declines by a factor of about e^{-1} – e^{-2} . Therefore, the delta function in divergence should be very small. To find p_{TROP} , ERA-Interim temperature data are used to locate the level of the troposphere where the temperature lapse rate first approaches zero over a depth of 2 km. In summary, ω_{Ek} is constructed such that it is zero at p_{SFC} , linearly increases to its maximum magnitude at p_{BL} , exponentially decays throughout the free troposphere, and is zero above p_{TROP} .

c. Calculation of the energetics and EEPE

The daily values of the Lorenz energy cycle (Lorenz 1955) are calculated according to a strictly spatial eddy formulation of the equations found in Peixoto and Oort (1974). Details on the equations that we employ may be found in appendix A. The following quantities are found: P_E , K_E , baroclinic conversion $C(P_M, P_E)$, eddy conversion $C(P_E, K_E)$, and barotropic conversion $C(K_E, K_M)$. Positive values of the conversion terms indicate a conversion from the first variable to the second variable within the parentheses. When calculating the energetics, a daily mass factor is derived to account for reanalysis pressure levels that fall below the terrain (e.g., Oort 1983).

To calculate $C_{\text{Ek}}(P_E, K_E)$, the generation of K_E due to Ekman pumping, ω_{Ek} found in Eqs. (1) and (2) is substituted into Eq. (A3). Since we are interested primarily in the generation of P_E due to Ekman pumping (EEPE), we define EEPE to be equivalent to $-C_{\text{Ek}}(P_E, K_E)$, that is, $C_{\text{Ek}}(K_E, P_E)$. Comparing the energetics of the two-layer QG model of Lee (2010b) and the formulation used by this study, $C_{\text{Ek}}(K_E, P_E)$ is equivalent to the third term on the right-hand side of Eq. (9) in Lee (2010b), since the thickness in that equation is equivalent to temperature in the atmosphere. Furthermore, the third term on the right-hand side of Eq. (8.2) in Lee (2010b), the eddy kinetic energy equation, is equivalent to the sum of frictional dissipation and $-C_{\text{Ek}}(K_E, P_E)$.

The energetic terms are integrated over the domain of the SH. Their climatologies are calculated and compared to the values computed by Li et al. (2007). Climatological values of EEPE are also calculated. There are several differences between the energetic calculations of this study and those of Li et al. First, this study employs higher-quality ERA-Interim data while Li et al. employed the 40-yr ECMWF Re-Analysis (ERA-40) and National Centers for Environmental Prediction (NCEP)–U.S. Department of Energy (DOE) reanalysis (NCEP2). Second, this study uses 33 years of data from 1979 to 2011, while Li et al. used 23 years of data from 1979 to 2001. Third, the integration in this study includes data up to the 1-hPa level, while Li et al. included data up to 10 hPa. Fourth, this study uses a strictly spatial formulation of the eddies, whereas Li et al. used a mixed space–time formulation. Fifth, this study evaluates the energetics on a daily basis, while Li et al. evaluated the data monthly.

Despite these differences, there is generally good agreement between the two sets of calculations. The energy values are generally within 10% of each other, and any differences may be attributed to the previously enumerated reasons. The energy conversion values of

$C(P_M, P_E)$ and $C(P_E, K_E)$ are also in agreement. However, this study finds values of $C(K_E, K_M)$ that are generally 2–3 times larger than the values computed by Li et al. (2007), a divergence that likely cannot be completely explained by the aforementioned reasons. After some investigation, it was determined that this divergence may possibly be attributed to the inclusion of a curvature term [second term on the right-hand side of Eq. (A5)] in this study's calculations. We find that if we remove this term from our calculations of $C(K_E, K_M)$, then our results more closely match those of Li et al. (2007).

d. Calculation of the vertical phase tilt

To calculate the daily phase difference between the upper (300 hPa) and lower (925 hPa) levels of the atmosphere, we decompose the geopotential at each level via spectral analysis into its component waves. This decomposition is performed daily in the longitudinal direction at each latitude and produces a series of waves that are a function of zonal wavenumber. As a result of this spectral analysis, each zonal wavenumber has a power and phase associated with it. We are only interested in zonal wavenumbers 3–10 because they contain most of the variance associated with the synoptic scale. For each of these eight zonal wavenumbers, we simply subtract the phases of the upper- and lower-level waves to calculate their phase difference as a function of zonal wavenumber. These eight phase differences are averaged, weighted by the power of the waves. To calculate the average phase difference of the storm track for a given hemisphere, only the phase differences for the latitudes between 30° and 70° are averaged, weighted by $\cos\phi$.

e. Composites

Composites of the energetics (which have been area averaged over the SH) are made against anomalous values of K_E and EEPE. The K_E and EEPE values are considered anomalous for this study if they deviate by more than one standard deviation from their climatological values on a given day. Climatological values are determined by averaging daily values from 1979 to 2011 and then applying a 1–2–1 smoothing scheme to the daily averages to produce an annual cycle. Specific details on the nature of each composite will be provided in the results section.

3. Results and discussion

a. Climatology of EEPE

The yearly and seasonal climatological values of EEPE and $C(P_E, K_E)$ are displayed in Table 1. As defined earlier, EEPE is equivalent to $C_{\text{Ek}}(K_E, P_E)$. Therefore,

TABLE 1. Seasonal and annual climatological means of EEPE and $C(P_E, K_E)$, averaged over the Southern and Northern Hemispheres, evaluated daily with ERA-Interim (1979–2011) data, during March–May (MAM), June–August (JJA), September–November (SON), and December–February (DJF). EEPE is equivalent to $C_{\text{Ek}}(K_E, P_E)$. Positive values of EEPE indicate the generation of P_E , whereas positive values of $C(P_E, K_E)$ indicate the generation of K_E . All units are watts per square meter.

Period	EEPE = $C_{\text{Ek}}(K_E, P_E)$		$C(P_E, K_E)$	
	SH	NH	SH	NH
MAM	−0.01	−0.10	2.58	2.08
JJA	0.02	−0.21	3.44	1.35
SON	−0.04	−0.13	2.83	2.12
DJF	−0.05	−0.07	1.91	3.12
Annual	−0.02	−0.13	2.69	2.17

positive values of EEPE found in Table 1 indicate the generation of P_E , whereas positive values of $C(P_E, K_E)$ indicate the generation of K_E . According to Table 1, Ekman pumping generates K_E at an average 0.13 W m^{-2} in the NH and 0.02 W m^{-2} in the SH. Despite the climatologically negative values of EEPE, it is found that when daily values of EEPE are mapped horizontally (not shown here) there are synoptic-scale regions where EEPE is positive. It may also be seen in Table 1 that EEPE reaches a maximum (minimum) in both hemispheres during their respective meteorological winters (summers). In fact, EEPE attains a positive value of 0.02 W m^{-2} in the SH during its winter that suggests that dissipative energization, if it exists, may be present during austral winter.

Further examination of Table 1 reveals that the values associated with EEPE are roughly one to two orders of magnitude smaller than the magnitudes associated with total $C(P_E, K_E)$. Despite this difference in magnitude, it will be shown that eddy life cycles have different characteristics when composited against anomalously positive or negative EEPE.

Figure 1 depicts the climatological values of EEPE during December–February (DJF) (Figs. 1a,c) and during June–August (JJA) (Figs. 1b,d). Superimposed on the figures are 25 and 15 m s^{-1} contours of the climatological zonal wind. Within the lower troposphere, Ekman pumping predominantly generates K_E ; within the mid- to upper troposphere of the midlatitudes, it predominantly generates P_E ; and near the tropopause, it predominantly generates K_E (Figs. 1a,b). Examining the SH during DJF (Figs. 1a,c), there is a particularly large maximum of EEPE near 52°S, which is slightly poleward of the SH's eddy-driven jet's climatological DJF position of approximately 48°S. This maximum of EEPE near 52°S is zonally symmetric (Fig. 1c). Similarly, the

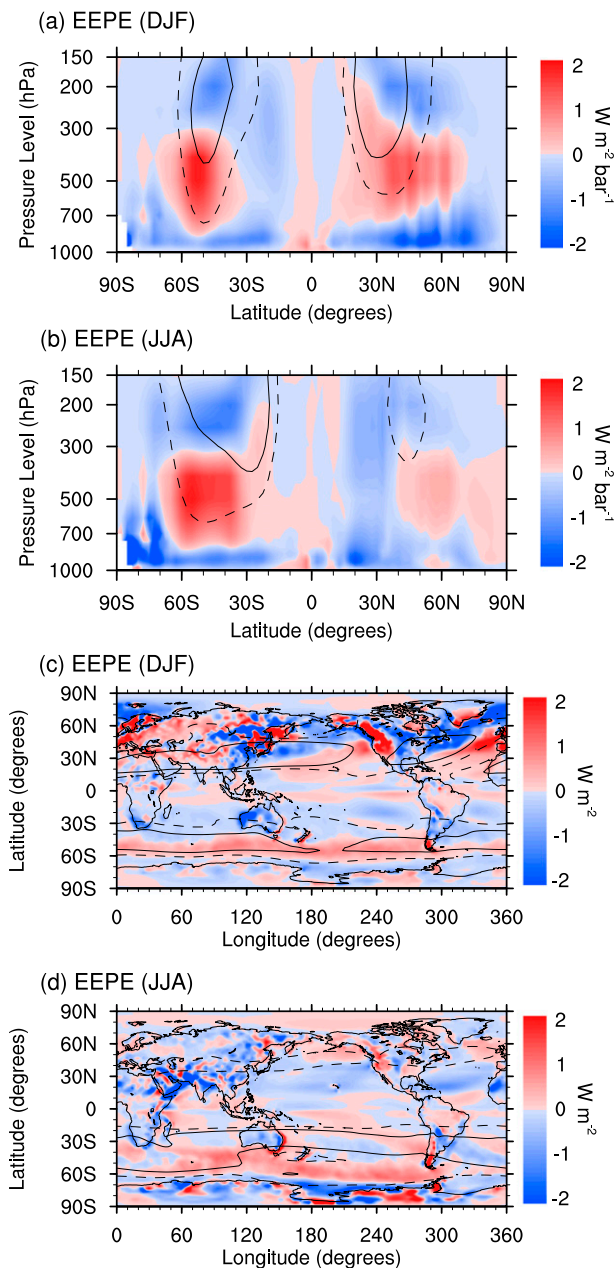


FIG. 1. The 1979–2011 climatological means of EEPE as a function of (a),(b) pressure level and latitude and (c),(d) latitude and longitude (i.e., the vertical integral of EEPE over all pressure levels, $g^{-1} \int \omega'_{EK} \alpha' dp$), during (a),(c) DJF and (b),(d) JJA. Positive (negative) values indicate the conversion from K_E to P_E (from P_E to K_E) as a result of Ekman pumping. Solid and dashed black contours correspond to the 25 and 15 m s^{-1} contours of the climatological zonal wind, respectively. Evaluated daily with ERA-Interim data.

maxima of EEPE in the SH during JJA (Fig. 1b) are located near 56° and 36°S , which are both slightly poleward of the climatological JJA positions of the eddy-driven jet ($\sim 52^\circ\text{S}$) and the subtropical jet ($\sim 30^\circ\text{S}$),

respectively. Again, the maximum of EEPE associated with the eddy-driven jet is zonally symmetric (Fig. 1d); however, the maximum of EEPE associated with the subtropical jet appears to have two longitudinally dependent maxima near 90°E and 80°W (Fig. 1d). Another interesting feature to note in Figs. 1a and 1b are the positive values of EEPE just to the south of the equator. It is not clear if this feature has physical meaning or is an artifact of uncertainties associated with the calculation of EEPE near the equator.

The vertical structure of EEPE (Figs. 1a,b) is dependent on the value of the parameters that we choose in Eq. (3). The results displayed throughout this study use a length scale L that corresponds to zonal wavenumber 6. This length scale yields an exponentially decaying vertical profile of ω_{EK} throughout the free troposphere with an e -folding depth of about 5–10 km. We test the sensitivity of EEPE to the value of L . Calculating ω_{EK} with shorter wavelengths yields a vertical profile of ω_{EK} such that ω_{EK} becomes trapped near the boundary layer. Figure 2 depicts various length scales that are tested. It may be seen that EEPE has a sharp maximum during JJA for L corresponding to zonal wavenumber 6. At both shorter and longer wavelengths, the peak in EEPE during JJA is more subdued. Thus, the numerical climatological values of EEPE that are presented in this study should be observed with caution. However, after performing various sensitivity tests, it is found that the annual cycle, the horizontal spatial structure of EEPE, and the remaining results of this study are not highly dependent on the length scale chosen. We perform an additional test where we calculate EEPE assuming uniform horizontal divergence in the free troposphere such that the magnitude of ω_{EK} linearly decreases between p_{BL} and p_{TROP} and find our results to be qualitatively unchanged.

b. Vertical phase tilt

The climatological vertical phase tilt of the SH between 30° and 70°S is found to be 50.1° with a standard deviation of 9.3° , such that the lower waves lead the upper waves. This climatological value of approximately $1/8$ wavelength is less than the $1/4$ -wavelength divider for the generation of P_E versus K_E by Ekman pumping found in Lee (2010b). However, it is not expected that a continuous atmosphere will have the same properties as a two-layer model. Anomalous EEPE is composited against days when the SH exhibits waves that are anomalously in phase (Fig. 3a) and anomalously out of phase (Fig. 3b). It is found that EEPE is anomalously positive (negative) when the SH storm track has an anomalously small (large) vertical phase tilt. These results confirm Lee (2010b)'s modeling results in which

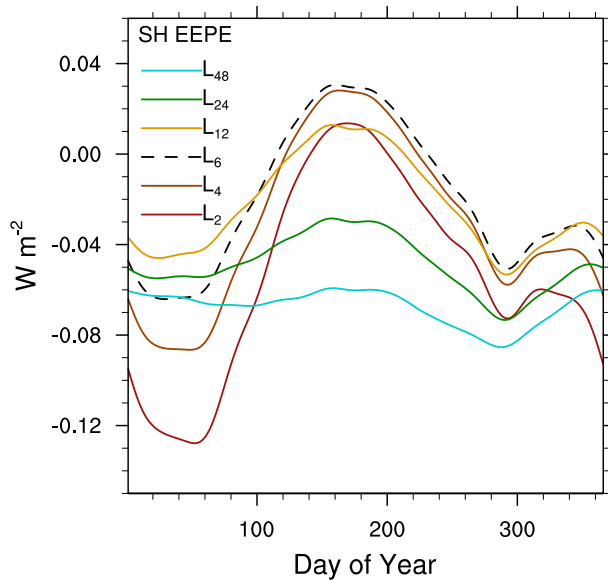


FIG. 2. Smoothed daily climatological values of EEPE averaged over the SH. Different curves correspond to different length scales L_n used in calculating the vertical profile of the Ekman pumping vertical velocity, such that L_n is the length of a latitudinal circle divided by $4n$. The dashed black curve corresponds to the length scale used in the results throughout this study, that is, the length scale of zonal wavenumber 6. Evaluated with ERA-Interim (1979–2011) data.

Ekman pumping favors the generation of P_E (K_E) when the upper and lower waves are anomalously in phase (out of phase).

c. Eddy life cycle composites

To evaluate the temporal placement of EEPE in the eddy life cycle, a series of lag-anomaly composites of the SH energetics are made against anomalously positive daily values of K_E in the SH at lag 0, such that only the peak values of K_E within a 7-day time period are chosen. This ensures that the peak amplitude of the eddy life cycle is found and results in 105 (113) days during DJF (JJA) being extracted from the 33-yr daily time series. These composites are denoted by K_E+ . It should be noted that choosing the peak amplitude of K_E within a 7-day time period does not distinguish between individual eddies within the storm track. Rather, it finds the days when the eddy amplitude of the entire SH is anomalously high. The left columns in Figs. 4 and 5 depict the SH eddy life cycle for K_E+ during DJF and JJA, respectively. There are peaks in baroclinic conversion $C(P_M, P_E)$ and eddy conversion $C(P_E, K_E)$ at short negative lags that are followed by peaks in P_E and K_E at lag 0 and a minimum of $-C(K_E, K_M)$ at lag +1. Negative values of $-C(K_E, K_M)$ imply positive values of $C(K_E, K_M)$, that is, barotropic decay. The observed eddy

life cycle may therefore be succinctly summarized as baroclinic growth followed by barotropic decay. This life cycle is entirely consistent within Lorenz's framework where energy flows from P_M to P_E to K_E to K_M and has been identified in both observations (Randel and Stanford 1985; Moon and Feldstein 2009) and idealized model calculations (Simmons and Hoskins 1978, 1980; Feldstein and Held 1989). Within this framework, Figs. 4p and 5p show that EEPE peaks at short positive lags, during the barotropic decay phase of the eddy life cycle.

Composites of the eddy life cycle based on anomalously positive and negative EEPE during summer (Fig. 4) and winter (Fig. 5) in the SH are now made. The middle columns in Figs. 4 and 5 depict lag anomaly composites of the energetics against anomalously positive values of EEPE at lag +2, given anomalously positive values of K_E at lag 0. These composites are denoted by $EEPE+|K_E+$. This results in 34 (46) days for DJF (JJA). In contrast, the right columns in Figs. 4 and 5 depict lag anomaly composites of the energetics against negative EEPE anomalies at lag +2, given anomalously positive values of K_E at lag 0. These composites are denoted by $EEPE-|K_E+$. This results in 31 (25) days for DJF (JJA). Therefore, the middle columns in Figs. 4 and 5 represent the eddy life cycle when the EEPE anomaly is greater than one standard deviation at lag +2, while the right columns in Figs. 4 and 5 represent the eddy life cycle when the EEPE anomaly is simply negative. The condition is relaxed in the negative case in order to provide a significant number of days to composite and is a direct result of EEPE anomalies having a positive mean near lag +2 during the eddy life cycle.

Comparing the DJF SH eddy life cycles of $EEPE+|K_E+$ and $EEPE-|K_E+$ (middle and right columns in Fig. 4, respectively), several features may be seen. First, values of P_E are similar at short lags, near the peak of the eddy life cycle, whereas K_E is slightly higher for $EEPE+|K_E+$. Eddy conversion $C(P_E, K_E)$ is larger for $EEPE-|K_E+$. The increase in generation of K_E through Ekman pumping may contribute to the observed increase of $C(P_E, K_E)$ because according to Eq. (A3), $C(P_E, K_E)$ is calculated using total ω , which includes ω_{Ek} . The $C(P_M, P_E)$ term is smaller for the $EEPE+|K_E+$ life cycles at positive lags, while the $-C(K_E, K_M)$ term has larger negative values at short positive lags for $EEPE-|K_E+$. Qualitatively, varying the strength of EEPE during DJF in the SH has only minor effects on eddy amplitude. However, there is evidence that eddy conversion, baroclinic conversion, and barotropic decay are smaller for $EEPE+|K_E+$ at short positive lags.

A comparison is now made between the JJA SH eddy life cycles of $EEPE+|K_E+$ and $EEPE-|K_E+$ (middle and right columns in Fig. 5, respectively). The K_E value

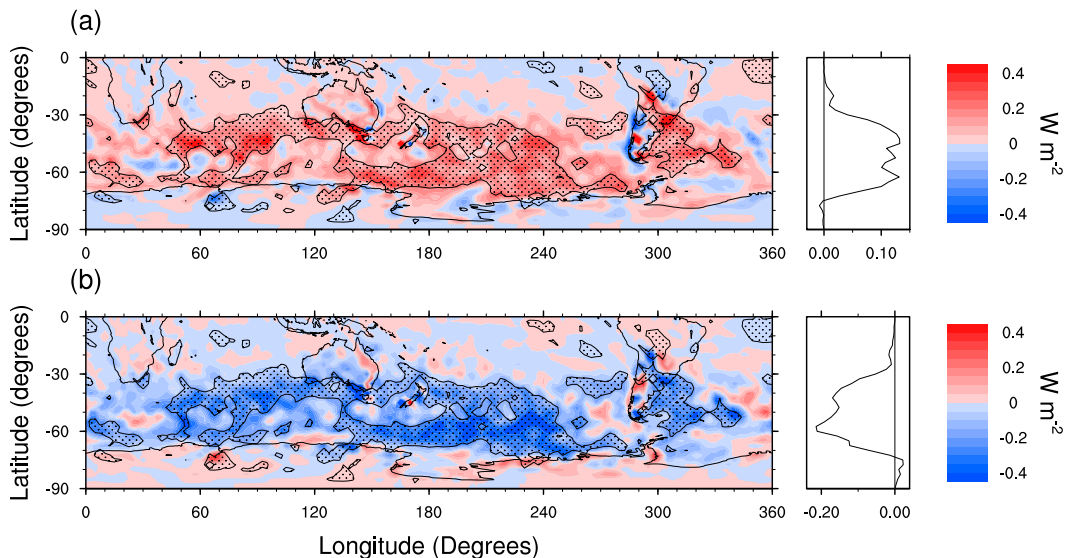


FIG. 3. (left) Southern Hemisphere composites of anomalous EEPE (as a function of latitude and longitude) on days when the anomalous phase difference between the upper (300 hPa) and lower (925 hPa) levels of the atmosphere between 30° and 70° S is (a) less than -1 standard deviation (1764 cases) and (b) greater than $+1$ standard deviation (1780 cases). The contoured stippled regions indicate areas of 95% confidence in the difference between the two composites evaluated with a t test. (right) Zonal means of anomalous EEPE. Evaluated with ERA-Interim (1979–2011) data.

is larger for $EEPE+ | K_E+$ near the peak of the eddy life cycle and at positive lags. The P_E value is persistently positive for $EEPE+ | K_E+$ at positive lags. The persistently positive values of P_E may be the result of the enhanced generation of P_E due to anomalously positive EEPE at lag $+2$. Both $C(P_E, K_E)$ and $C(P_M, P_E)$ are smaller at short positive lags for $EEPE+ | K_E+$. It may also be seen that $C(K_E, K_M)$ is smaller for $EEPE+ | K_E+$. This reduced barotropic decay seemingly accounts for the higher values of K_E seen in $EEPE+ | K_E+$ life cycles.

A summary of the main results of Figs. 4 and 5 is now given. 1) When eddy life cycles are composited against positive EEPE, K_E is larger, particularly during JJA. 2) Life cycles with anomalously positive EEPE do not exhibit enhanced $C(P_M, P_E)$ during either JJA or DJF. This lack of enhancement of baroclinic conversion in reanalysis data runs counter to the dissipative energization results of Lee (2010b). 3) Life cycles with anomalously positive EEPE have smaller $C(K_E, K_M)$. This muted barotropic decay likely accounts for the higher values of K_E found during $EEPE+ | K_E+$ life cycles.

d. Investigation of baroclinic conversion

An outstanding question that remains is why there is no observed enhancement of baroclinic conversion for eddies with anomalously positive EEPE—a result that runs counter to the findings of Lee (2010b). To address this question, we decompose baroclinic conversion into

the sum of four competing effects: the baroclinicity effect, the v' effect, the T' effect, and the vertical-phase-tilt effect. We then consider the relative influences of these four competing effects to see which accounts for the lack of enhancement of baroclinic conversion for $EEPE+ | K_E+$.

The formula for baroclinic conversion is given by Eq. (A4). From this formulation, we derive (in detail in appendix B) the following expression for anomalous baroclinic conversion per unit mass:

$$\delta(B\overline{v'T'}) \cong \delta B(\overline{v'T'})_C + \delta s_v(s_T)_C r_C B_C + \delta s_T(s_v)_C r_C B_C + \delta r(s_v)_C(s_T)_C B_C. \quad (4)$$

In Eq. (4), B is baroclinicity and includes the effects of stability and the zonal-mean meridional temperature gradient (e.g., Rivière and Joly 2006); $\overline{v'T'}$ is the zonal mean of the meridional eddy heat flux. Mathematically, $\overline{v'T'}$ is a covariance, and therefore $\overline{v'T'} = s_v s_T r$, where s_v and s_T are the sample standard deviations in the longitudinal direction of v and T , respectively, and r is the longitudinal correlation between v and T . Variables with the subscript C are smoothed daily climatologies and variables with δ are deviations from smoothed daily climatologies. Therefore, Eq. (4) relates anomalous baroclinic conversion per unit mass to the sum of four terms, each of which contains one anomalous variable:

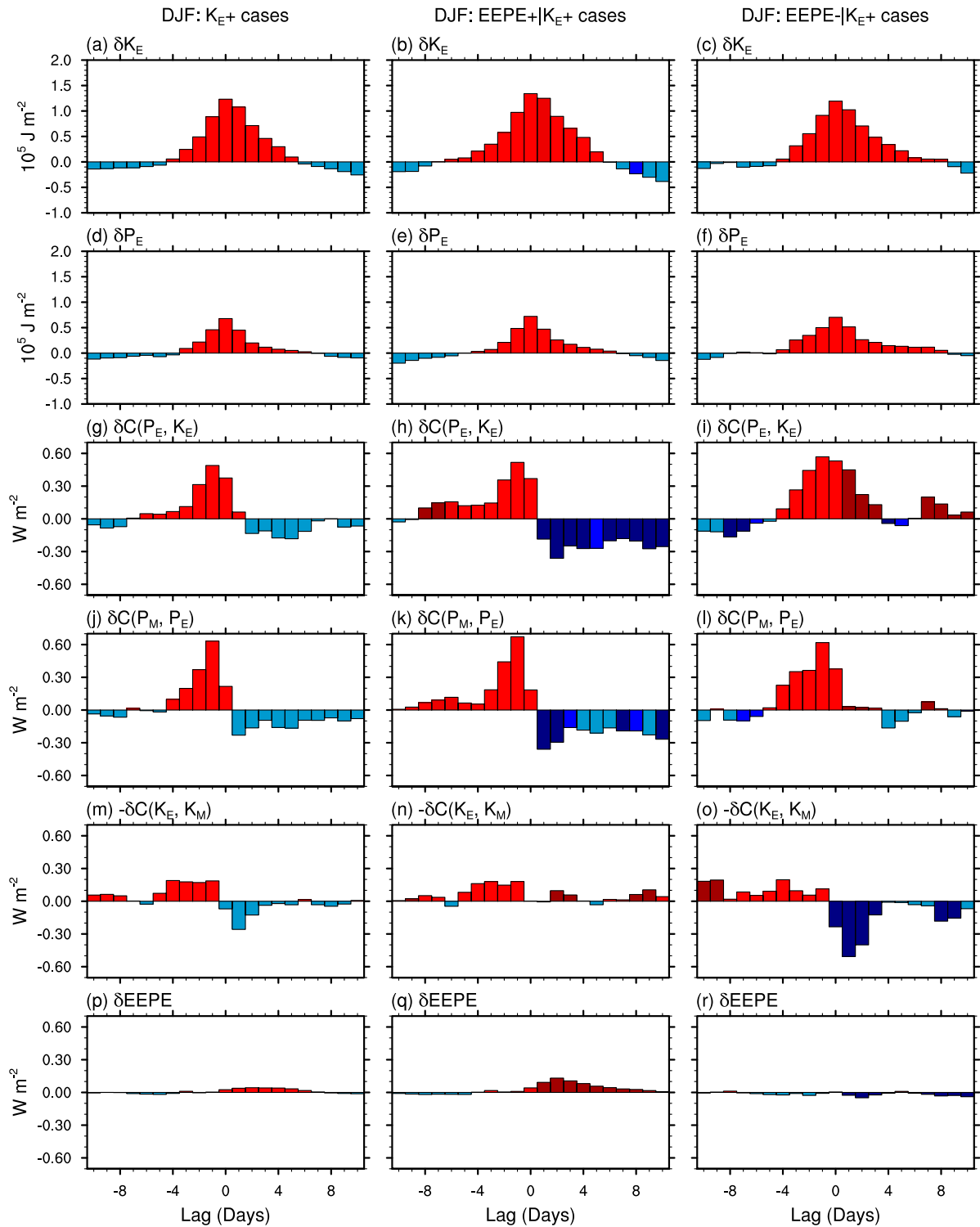


FIG. 4. Southern Hemisphere lag anomaly composites during DJF of (a)–(c) δK_E , (d)–(f) δP_E , (g)–(i) $\delta C(P_E, K_E)$, (j)–(l) $\delta C(P_M, P_E)$, (m)–(o) $-\delta C(K_E, K_M)$, and (p)–(r) $\delta EEPE$, composited against days that satisfy the selection criteria for (left) K_{E+} (105 cases), (middle) $EEPE+ | K_{E+}$ (34 cases), and (right) $EEPE- | K_{E+}$ (31 cases). The criteria for selecting these days are described in the text. The δ in front of each term signifies that the composites are of anomalies from smoothed daily climatologies. Dark (medium) shades of red and blue found in the middle and right columns represent 95% (90%) confidence in the difference between the two composites evaluated with a t test. Evaluated with ERA-Interim (1979–2011) data.

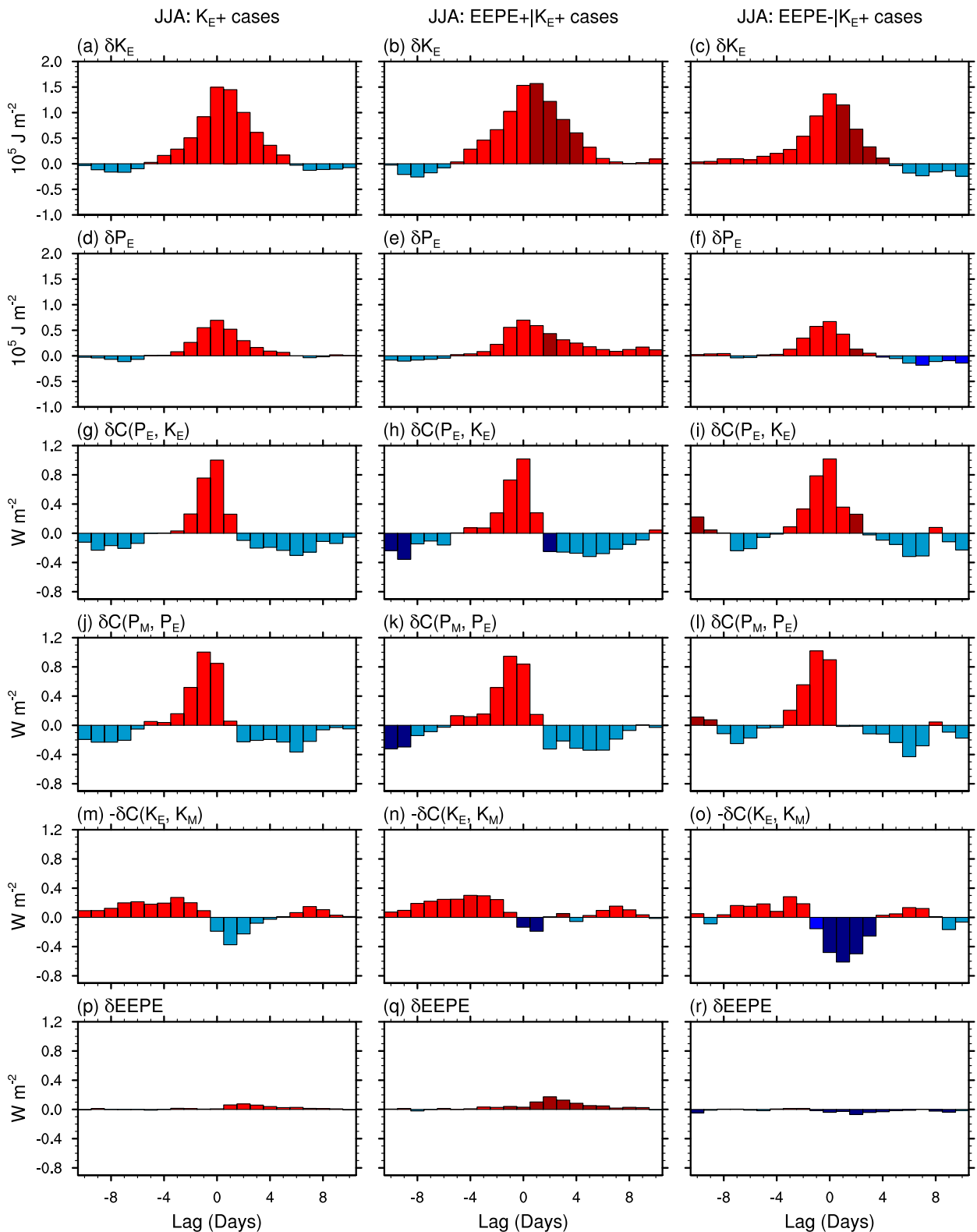


FIG. 5. As in Fig. 4, but only during JJA at lag 0: (left) 113, (middle) 46, and (right) 25 cases.

δB , δs_v , δs_T , and δr . These four terms respectively represent the baroclinicity effect, the v' effect, the T' effect, and the vertical-phase-tilt effect.

Regarding these four effects, we expect EEPE to have an intuitive relationship to two of them, namely, the T' effect and the vertical-phase-tilt effect. When EEPE is anomalously positive, there is a generation of P_E that implies a growth of T' and hence positive δs_T (the T' effect). Furthermore, when EEPE is anomalously positive, we have shown that the upper and lower waves are anomalously in phase, which implies negative δr (the vertical-phase-tilt effect). To account for the lack of enhancement of baroclinic conversion for EEPE+| K_E +, it is hypothesized that the vertical-phase-tilt effect dominates the T' effect. We calculate these two effects, while also considering the possible influences of the baroclinicity effect and the v' effect.

The five terms in Eq. (4) are calculated daily, integrated over the SH, and then divided by the surface area of the SH. Each term is then composited against K_E +, EEPE+| K_E +, and EEPE-| K_E + for DJF and JJA (Figs. 6 and 7). To check the validity of the approximation given in Eq. (4), the four terms on the right-hand side of Eq. (4) are summed (Figs. 6m-o and 7m-o) and compared with $\delta(BvT')$ (Figs. 6p-r and 7p-r). It can be seen that the sum of the four effects strongly resembles anomalous baroclinic conversion. The small differences that exist may likely be attributed to small terms that are neglected during the derivation of Eq. (4). For example, $\delta(BvT')$ only includes the meridional heat flux term of Eq. (A4), while neglecting the vertical eddy heat flux term, which we calculate to be small. Thus, although Figs. 6p-r and 7p-r strongly resemble total baroclinic conversion (Figs. 4j-l and 5j-l), they are not perfectly identical.

Regarding Figs. 6a-l and 7a-l, the following results are seen. The first rows, which represent the baroclinicity effect, have the smallest magnitude of the four effects. The second rows, which represent the v' effect, have a slightly larger magnitude than the third rows that represent the T' effect. The fourth rows, which represent the vertical-phase-tilt effect, generally have the largest amplitudes with positive anomalies at negative lags and negative anomalies at positive lags. This is consistent with an eddy life cycle in which the upper- and lower-level waves become more in phase as the eddy amplitude peaks and then weakens.

Although small differences may be seen between the two life cycles with respect to the baroclinicity effect, the T' effect, and the v' effect, the most noticeable difference in the two eddy life cycles of EEPE+| K_E + and EEPE-| K_E + for both DJF and JJA involves the vertical-phase-tilt effect. It can be seen for EEPE+| K_E + that

the vertical-phase-tilt effect is more anomalously negative at small positive lags than for EEPE-| K_E + (Figs. 6k,l and 7k,l). This result is consistent with our earlier result that anomalously positive (negative) EEPE is associated with an anomalously small (large) vertical phase tilt. It may also be seen that the v' effect and the T' effect are slightly more anomalously positive (particularly for JJA) at small positive lags for EEPE+| K_E + than for EEPE-| K_E + (Figs. 6e,f,h,i and 7e,f,h,i). With respect to the T' effect, this result may possibly be attributed to the composites being based on anomalous EEPE at lag +2 and anomalously positive EEPE by definition implies an enhanced conversion from K_E to P_E and therefore an enhancement of T' . Comparing the two eddy life cycles, it is evident that the vertical-phase-tilt effect has a change in magnitude that dominates over the change in magnitudes of the baroclinicity effect, the v' effect, and the T' effect. Thus, for EEPE+| K_E +, despite a positive contribution to baroclinic conversion due to a small enhancement of the v' effect and the T' effect, the vertical-phase-tilt effect's contribution to baroclinic conversion is more negative at short lags than for EEPE-| K_E +. Therefore, we do not see an enhancement of baroclinic conversion for eddy life cycles with anomalously positive EEPE.

e. Investigation of barotropic conversion

An additional outstanding question that needs to be addressed is why barotropic decay is smaller for eddies associated with anomalously positive EEPE. Using a two-layer QG model, Lee and Held (1991), Lachmy and Harnik (2009), and Lee (2010a) all found a reduction in barotropic decay that led to an overall amplification of the eddies. In the study performed by Lee and Held (1991), it was found that the formation of reflecting critical latitudes at the upper layer, caused by the homogenization of potential vorticity within the critical latitudes, led to less absorption of the wave and subsequent destabilization. Lachmy and Harnik (2009) showed that as their one-wave solution grew, the potential vorticity gradient on the inner sides of upper-layer critical levels was reduced. Lee (2010a) demonstrated wave amplification via muted barotropic decay through a reduction in the horizontal shear of the zonal wind. Since barotropic decay is muted in the EEPE+| K_E + life cycle, we ask ourselves if processes similar to those found in the modeling studies are occurring for EEPE+| K_E +. The remainder of this section is devoted to answering this question by examining the eddy structures and background flows associated with the eddy life cycles of EEPE+| K_E + and EEPE-| K_E +

One-point correlation maps of the v wind at 300 hPa are constructed in order to reveal the eddy structures

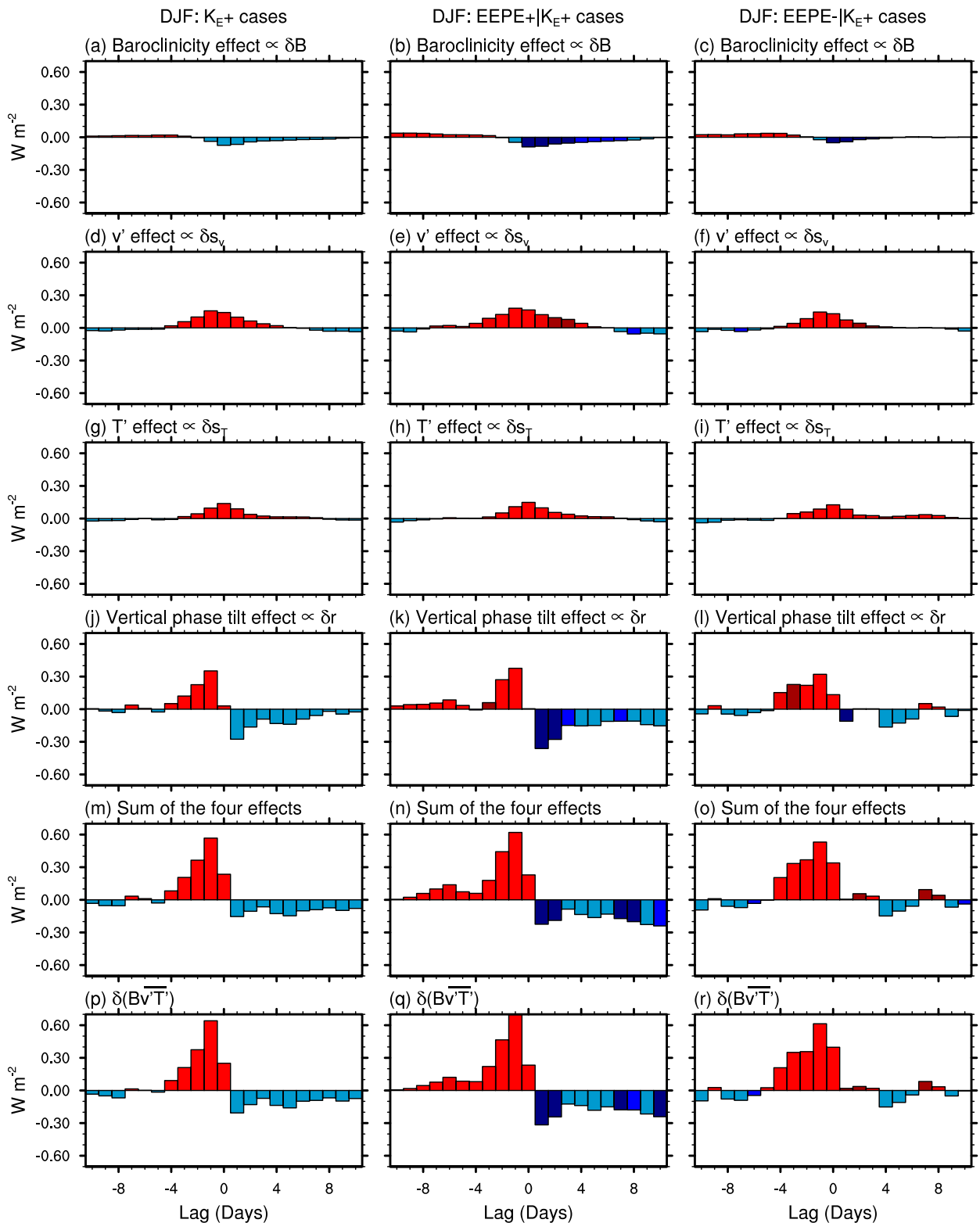


FIG. 6. Southern Hemisphere lag composites during DJF of (a)–(c) $\int [\delta B(\overline{vT})_C] dm$; (d)–(f) $\int [\delta s_v(s_T)_{CrCB_C}] dm$; (g)–(i) $\int [\delta s_T(s_v)_{CrCB_C}] dm$; (j)–(l) $\int [\delta r(s_v)_C(s_T)_CB_C] dm$; (m) sum of (a),(d),(g),(j); (n) sum of (b),(e),(h),(k); (o) sum of (c),(f),(i),(l); and (p)–(r) $\int [\delta(Bv\overline{T})] dm$, composited against days that satisfy the selection criteria for (left) K_{E+} (105 cases), (middle) $EEPE+|K_{E+}$ (34 cases), and (right) $EEPE-|K_{E+}$ (31 cases). Dark (medium) shades of red and blue found in the middle and right columns represent 95% (90%) confidence in the difference between the two composites evaluated with a t test. The criteria for selecting these days are described in the text. Evaluated with ERA-Interim (1979–2011) data.

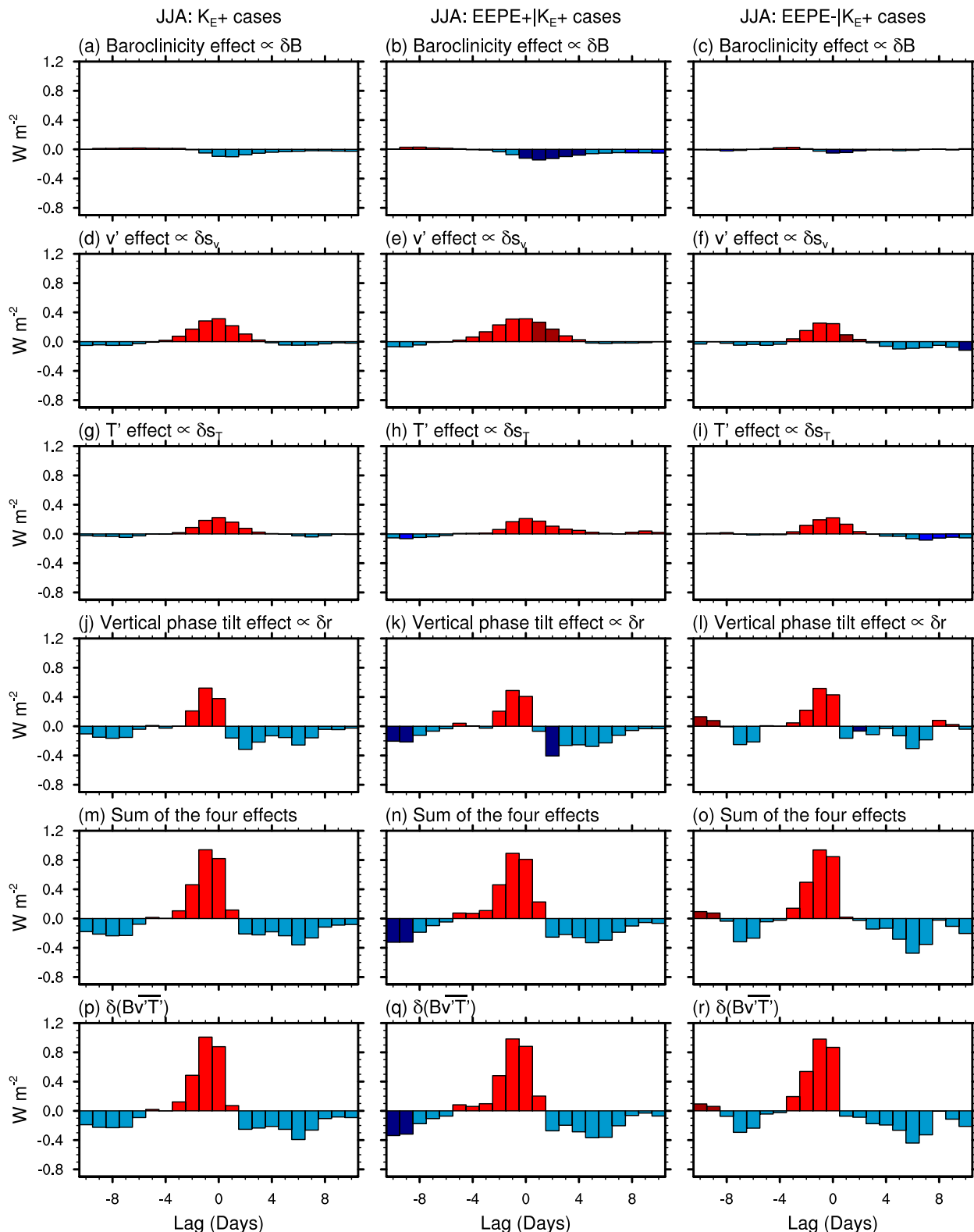


FIG. 7. As in Fig. 6, but only during JJA at lag 0: (left) 113, (middle) 46, and (right) 25 cases.

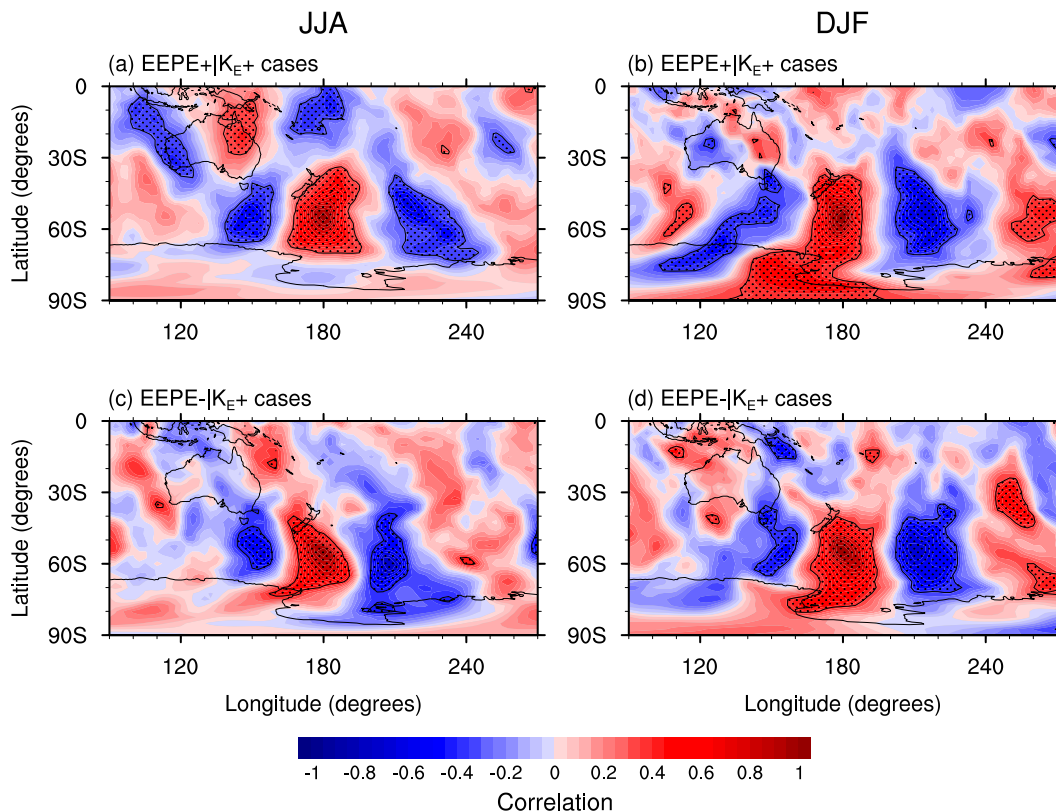


FIG. 8. One-point correlation maps of the v wind field at 300 hPa correlated against the v wind at 55°S , 180° during (a),(c) JJA and (b),(d) DJF. The correlations are made using days when (a),(b) EEPE+ $|K_E+$ (46 JJA and 34 DJF cases) and (c),(d) EEPE- $|K_E+$ (25 JJA and 31 DJF cases). The criteria for selecting these days are described in the text. The contoured stippled regions indicate areas of 95% confidence that the correlation coefficient is significant. Evaluated with ERA-Interim (1979–2011) data.

associated with EEPE+ $|K_E+$ and EEPE- $|K_E+$ (Fig. 8). The point chosen for analysis during both JJA and DJF is 55°S , 180° . As seen in Figs. 1c and 1d, this point lies on a local maximum in EEPE, near the eddy-driven jet. Additional points are tested (not shown here) and found to have qualitatively similar structures to the point located at 55°S , 180° . Figures 8a and 8c reveal that the eddies associated with EEPE+ $|K_E+$ during JJA have a more distinct and discontinuous spatial structure (i.e., discrete) than those associated with EEPE- $|K_E+$. Evidence of the discrete nature of the EEPE+ $|K_E+$ eddies may be seen near 35°S , where the sign of the v wind changes abruptly (Fig. 8a). In contrast, the eddy structure associated with EEPE- $|K_E+$ is more of a continuum with individual eddies having a tilted, boomerang structure. Therefore, the eddies associated with EEPE- $|K_E+$ are more conducive to eddy momentum flux convergence $-\partial_y \overline{u'v'} > 0$ (and an acceleration of the zonal wind) than the eddies associated with EEPE+ $|K_E+$. This result is consistent with our earlier result that EEPE+ $|K_E+$ is associated with muted barotropic decay. Comparing the two eddy life cycles for

DJF (Figs. 8b,d), it is not as readily apparent that the eddy structure for EEPE- $|K_E+$ is more conducive to eddy momentum flux convergence than EEPE+ $|K_E+$.

Continuing to address why barotropic decay is muted for eddies associated with positive EEPE, the refractive index, as derived from the linearized nondivergent barotropic model, is now calculated such that $n^2 = (\beta - \partial_{yy}\overline{u})(\overline{u} - c)^{-1} - k^2$, where $\beta = df/dy$, c is zonal phase speed, k is zonal wavenumber, and \overline{u} is the zonal mean of the zonal wind (e.g., Matsuno 1970; Karoly and Hoskins 1982; Palmer 1982). The refractive index is calculated as a function of latitude and lag day for EEPE+ $|K_E+$ and EEPE- $|K_E+$ at 300 hPa. The values substituted for c are derived from one-point correlation maps similar to those in Fig. 8. The values substituted for k are derived from a Fourier analysis of streamfunction at 300 hPa (Figs. 9a,b) and are averaged over the latitudinal band from 30° to 60°S from lag 0 to +4. To estimate the zonal phase speeds, we correlate the lag -1 and lag +1 v wind field against the v wind at lag 0 at four different points, spread 90° longitude apart along the SH eddy-driven jet. From these one-point

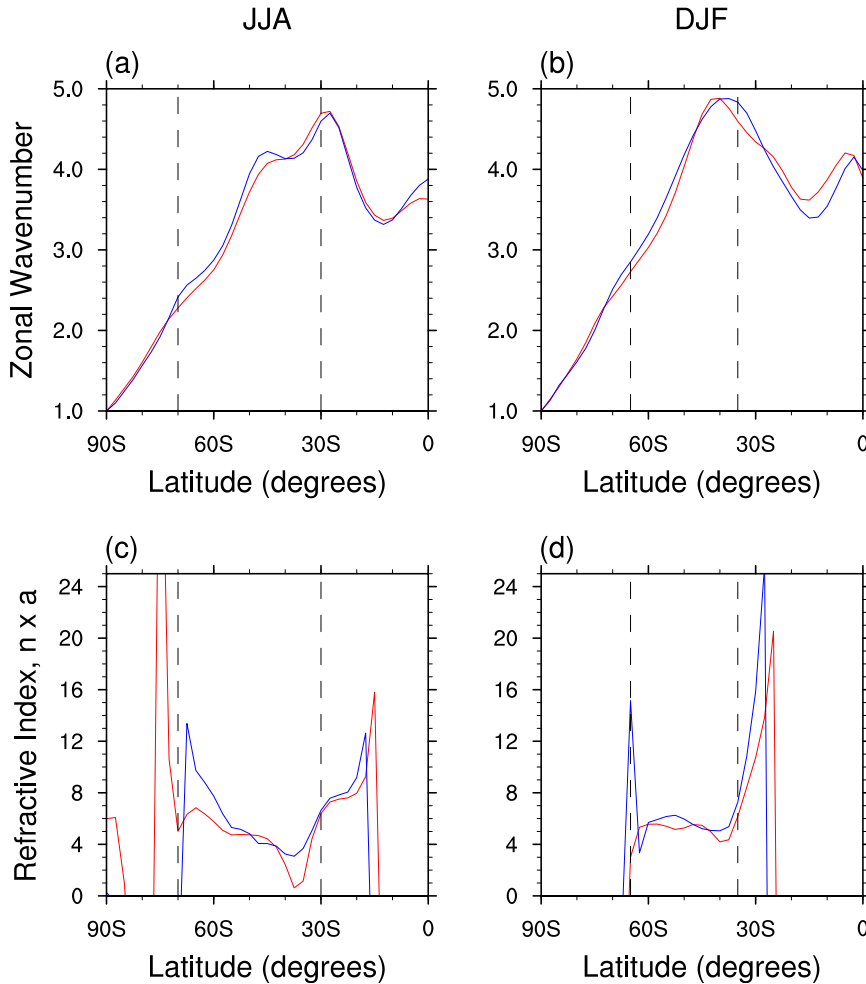


FIG. 9. Pentad average of the lag 0 to lag +4 composites of (a),(b) zonal wavenumber and (c),(d) nondimensionalized refractive index as functions of latitude at 300 hPa. Only values of $n \times a$ that correspond to $n^2 > 0$ are plotted. Dashed vertical lines represent the poleward and equatorward extents of the storm track, as estimated using climatological values of K_E during (a),(c) JJA and (b),(d) DJF. Red and blue lines represent the composites made against days that satisfy the selection criteria for $EEPE+|K_E+$ (46 JJA and 34 DJF cases) and $EEPE-|K_E+$ (25 JJA and 31 DJF cases), respectively. The criteria for selecting these days are described in the text. Evaluated with ERA-Interim (1979–2011) data.

correlation maps (not shown here), the zonal phase speed of the eddies may be inferred from their longitudinal displacement over the 48-h period. The inferred phase speeds from the four different points are then averaged. It is found that $EEPE+|K_E+$ has a phase speed of about 8.8 ms^{-1} during both DJF and JJA, while $EEPE-|K_E+$ exhibits phase speeds of about 11.1 and 10.8 ms^{-1} during DJF and JJA, respectively. Therefore, eddies associated with $EEPE-|K_E+$ have phase speeds approximately 25%–30% faster than eddies associated with $EEPE+|K_E+$. The slower phase speed for $EEPE+|K_E+$ raises the possibility that the waves are bounded by turning points before reaching their critical latitudes.

Figures 9c and 9d show the nondimensionalized refractive index (multiplied by the radius of Earth), averaged over the pentad of days from lag 0 to lag +4. Negative values (not depicted) indicate where the refractive index $n^2 < 0$. These figures reveal that during DJF the critical latitude in the subtropics is more distant from the midlatitude storm track for $EEPE+|K_E+$ than $EEPE-|K_E+$. It is reasonable to expect that wave absorption by critical latitudes would be more effective if the critical latitudes were closer to the storm-track region. Therefore, it may be that the relatively muted barotropic decay for $EEPE+|K_E+$ is due to its more distant critical latitude. We also investigate if the potential

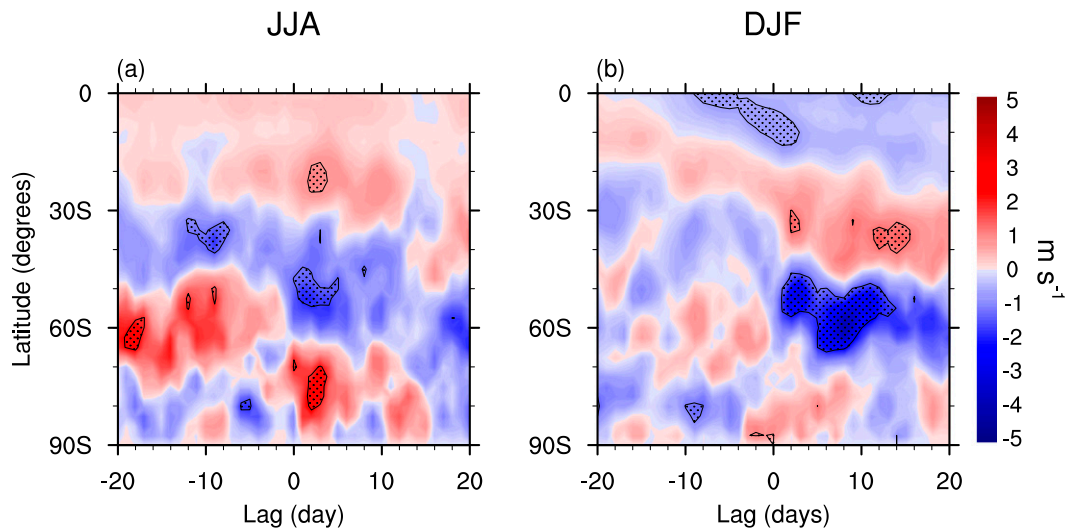


FIG. 10. Difference (as a function of latitude and lag day) between the composites of the mass-weighted vertical average of \bar{u} made against days that satisfy the selection criteria for $EEPE+|K_{E+}$ (46 JJA and 34 DJF cases) and $EEPE-|K_{E+}$ (25 JJA and 31 DJF cases) during (a) JJA and (b) DJF. The criteria for selecting these days are described in the text. Positive values indicate that the mass-weighted vertical average of \bar{u} is higher for $EEPE+|K_{E+}$ than $EEPE-|K_{E+}$. The contoured stippled regions indicate areas of 95% confidence in the difference between the two composites evaluated with a t test. Evaluated with ERA-Interim (1979–2011) data.

vorticity gradient at the critical latitudes is smaller for $EEPE+|K_{E+}$, but there is no appreciable difference and the values are not close to zero (not shown). Therefore, at least within linear theory, we cannot conclude that a reflecting critical latitude is the reason for the muted barotropic decay for $EEPE+|K_{E+}$.

During JJA, we again find that the location of the subtropical critical latitude is more distant from the storm-track region. However, Fig. 9c suggests that the presence of an evanescent region centered around 40°S may account for the subdued barotropic decay for $EEPE+|K_{E+}$ and would lessen the importance of the subtropical critical latitude. The eddy structure shown in Fig. 8a supports this possibility because it can be seen that the discrete eddies rapidly decay at the latitude of the evanescent region. While the refractive index for $EEPE-|K_{E+}$ also has a local minimum in this region, its value is not as small. Thus, the horizontal eddy structure and the corresponding refractive index collectively suggest that the muted barotropic decay for $EEPE+|K_{E+}$ during JJA may be caused by the equatorward side of the storm track being bounded by a turning latitude with a near-zero refractive index and not because of a reflecting critical latitude (i.e., not because of a near-zero potential vorticity gradient at the critical latitude).

The differences in refractive index between $EEPE-|K_{E+}$ and $EEPE+|K_{E+}$ are attributable to their difference in both phase speed and the 300-hPa

zonal-mean zonal wind. Because phase speed is directly proportional to $\{\bar{u}\}$, the mass-weighted vertical average of \bar{u} , it may be that $\{\bar{u}\}$ is smaller for $EEPE+|K_{E+}$. Figure 10 indeed reveals that beginning near lag -2 near the center of the storm track (50°S during JJA and 55°S during DJF) that $\{\bar{u}\}$ is less for $EEPE+|K_{E+}$ than $EEPE-|K_{E+}$. This result is consistent with the larger barotropic conversion exhibited by $EEPE-|K_{E+}$ life cycles. Furthermore, the positive values that flank these regions imply a reduction in the horizontal shear of $\{\bar{u}\}$ for $EEPE+|K_{E+}$. The reason why $\{\bar{u}\}$ is less for $EEPE+|K_{E+}$ near the center of the storm track is beyond the scope of this study, and we plan to address this question in a future study.

Concluding our investigation of barotropic decay, it is found that eddies associated with $EEPE+|K_{E+}$ have a discrete spatial structure that is not amenable to eddy momentum flux convergence (and hence barotropic decay). They are also associated with slower phase speeds. An examination of the refractive index reveals that the critical latitudes for $EEPE+|K_{E+}$ are farther away from the storm-track region due to the smaller phase speeds at the center of the storm track and larger $\{\bar{u}\}$ on the flanks of the storm track. This broad meridional range where waves are allowed to propagate is also not amenable to barotropic decay. During JJA when the zonal wind structure is more complex due to the coexistence of the subtropical and eddy-driven jets, the $EEPE+|K_{E+}$ eddies are bounded by an evanescent

region on their equatorward side. Therefore, the location of the critical latitude may not account for the difference in barotropic decay. In both cases and both seasons, we did not find any evidence of reflecting critical latitudes. Furthermore, a reduction (enhancement) of $\{\bar{u}\}$ near the center (flanks) of the storm track for $EEPE+|K_E+$ implies a reduction in the horizontal shear of \bar{u} and reduced barotropic decay, reminiscent of Lee (2010a).

4. Conclusions and future work

In the framework of the Lorenz energy cycle, the climatological characteristics of EEPE are evaluated. EEPE has an annual cycle that is maximized (minimized) during a given hemisphere's winter (summer) season. Over the course of an entire year, EEPE is negative in both hemispheres, except in the SH during JJA. However, there are regions of positive values of EEPE found in the storm tracks of each hemisphere. It is found that when the SH storm track is anomalously in phase (out of phase) in the vertical, EEPE is predominantly positive (negative). In the context of the eddy life cycle, EEPE peaks shortly after the peak eddy amplitude. For those eddies during JJA in the SH where EEPE is observed as anomalously positive (negative), there are larger (smaller) values of P_E and K_E . Baroclinic conversion is smaller in eddies with anomalously positive EEPE. Furthermore, barotropic decay is muted for eddies with anomalously positive EEPE.

To account for the lack of enhancement of baroclinic conversion for $EEPE+|K_E+$ life cycles, which runs counter to Lee (2010b), it is found that an anomalously small vertical phase tilt plays a leading role. Lee (2010b) found that the enhancement of baroclinic conversion occurs in the parameter space where total eddy energy increases with increasing Ekman damping. Therefore, it is possible that the model's parameter space relevant for the atmosphere is the region where eddy energy decreases with increasing Ekman damping.

Rather than this dissipative energization, it is shown for $EEPE+|K_E+$ life cycles that barotropic decay is muted, and this accounts for the larger eddy kinetic energy. This muted barotropic decay amplifies the eddies, which is consistent with several modeling studies (Lee and Held 1991; Lachmy and Harnik 2009; Lee 2010a). However, unlike in the models, we find no evidence of reflecting critical latitudes playing a role. Instead, a wave structure with no meridional tilt (which hints at wave reflection) is found only for $EEPE+|K_E+$ during JJA, but this structure coincides with the presence of an evanescent region on the equatorward side of the storm track. Physically, it may be that the muted

barotropic decay results in an atmosphere more amenable to positive EEPE by leaving behind large-amplitude upper-level (tropospheric) waves. From a potential vorticity perspective (Hoskins et al. 1985), we expect that circulations induced by these large-amplitude upper-level potential vorticity anomalies dominate throughout the troposphere. As a result, the waves will become more barotropic and hence be amenable to positive EEPE.

Several outstanding questions remain and will be addressed in future studies. 1) The climatological distribution of EEPE in the NH (Fig. 1) has an abundance of features that merit further investigation. Future work will investigate these features using a storm-scale perspective as opposed to a Lorenz global-scale perspective. 2) It was found by Kim and Lee (2004) that the interjet is associated with waves that have a smaller phase speed (and therefore longer waves with less vertical tilt). Because positive EEPE is also associated with slowly propagating waves, the relationship between EEPE and the interjet should be investigated. 3) The relationship of EEPE to tropical convection should be examined. Since tropical convection plays a large role in driving the background flow, the sign of EEPE may be more a function of tropical convection rather than internal variability. 4) Eddies are the primary drivers of climate in the midlatitudes. Therefore, long-term variability of EEPE should be explored in the context of a changing climate. The greater longevity of the eddy life cycle, as evidenced by $EEPE+|K_E+$ during JJA, may be relevant for extreme weather.

Acknowledgments. This study was supported by the National Science Foundation under Grant ATM-1139970 and by Seoul National University, South Korea. Valuable comments from Steven Feldstein, Michael Goss, and three anonymous reviewers helped improve this manuscript. All coding was performed using the National Center for Atmospheric Research Command Language (Brown et al. 2013).

APPENDIX A

Calculation of the Energetics

The following energy equations are obtained from Peixoto and Oort (1974) and are modified such that only the spatial eddy component is retained. The transient eddies are not computed because we are calculating the energetics daily using only the 0000 UTC time step. Furthermore, the time means found in the original equations are simply substituted with the daily value at 0000 UTC. Therefore, the modified equations are as follows:

$$P_E = \frac{c_p}{2} \int \gamma \overline{T'^2} dm, \quad (\text{A1})$$

$$K_E = \frac{1}{2} \int \overline{u'^2 + v'^2} dm, \quad (\text{A2})$$

$$C(P_E, K_E) = - \int \overline{\omega' \alpha'} dm, \quad (\text{A3})$$

$$C(P_M, P_E) = -c_p \int \gamma \overline{v'T'} \frac{1}{a} \frac{\partial \overline{T}}{\partial \varphi} dm - c_p \int p^{-\kappa} \overline{\omega'T'} \frac{\partial(\gamma p^\kappa \overline{T'})}{\partial p} dm, \quad \text{and} \quad (\text{A4})$$

$$C(K_E, K_M) = \int \frac{\overline{u'v'}}{a} \frac{\partial \overline{u}}{\partial \varphi} dm + \int \overline{u'v'} \tan \varphi dm + \int \overline{v'^2} \frac{1}{a} \frac{\partial \overline{v}}{\partial \varphi} dm + \int \overline{u'\omega'} \frac{\partial \overline{u}}{\partial p} dm + \int \overline{v'\omega'} \frac{\partial \overline{v}}{\partial p} dm - \int \overline{v'u'^2} \frac{\tan \varphi}{a} dm, \quad (\text{A5})$$

where $\gamma = -\theta R_d T^{-1} c_p^{-1} p^{-1} (\partial \overline{\theta} / \partial p)^{-1}$ is a stability factor, $dm = a^2 g^{-1} \cos \varphi d\lambda d\varphi dp$ is an element of mass, and $\kappa = R_d / c_p$. Furthermore, u is zonal wind, v is meridional wind, ω is vertical velocity, p is pressure, α is specific volume, T is temperature, θ is potential temperature, φ is latitude, λ is longitude, c_p is the specific heat of air at constant pressure, R_d is the ideal gas constant for dry air, a is the radius of Earth, and g is the acceleration of gravity. Overbars denote zonal averages, primes denote deviations from a zonal average, tildes denote meridional averages, and double primes denote deviations from a meridional average.

APPENDIX B

Decomposition of Baroclinic Conversion

Baroclinic conversion equation [Eq. (A4)] is the sum of a meridional eddy heat flux term and a vertical eddy heat flux term. Computing both terms, we find that the vertical eddy heat flux term is generally more than one order of magnitude smaller than the meridional eddy heat flux term, and it is therefore neglected. The quantity inside the integral of the meridional eddy heat flux term may be written as

$$B \overline{v'T'} = (B_C + \delta B) [(\overline{v'T'})_C + \delta(\overline{v'T'})], \quad (\text{B1})$$

where $B = -c_p \gamma a^{-1} \partial_\varphi \overline{T}$ may be viewed as baroclinicity (e.g., Rivière and Joly 2006). Variables with the subscript C are smoothed daily climatologies, and variables

with δ are deviations from smoothed daily climatologies. Separating the left-hand side of Eq. (B1) into climatological and anomalous components, while multiplying through the right-hand side, yields

$$(B \overline{v'T'})_C + \delta(B \overline{v'T'}) = B_C (\overline{v'T'})_C + \delta B (\overline{v'T'})_C + \delta(\overline{v'T'}) B_C + \delta B \delta(\overline{v'T'}). \quad (\text{B2})$$

Taking the climatological mean of Eq. (B2) produces the following two equations:

$$(B \overline{v'T'})_C = B_C (\overline{v'T'})_C + [\delta B \delta(\overline{v'T'})]_C \quad \text{and} \quad (\text{B3})$$

$$\delta(B \overline{v'T'}) = \delta B (\overline{v'T'})_C + \delta(\overline{v'T'}) B_C + \delta B \delta(\overline{v'T'}) - [\delta B \delta(\overline{v'T'})]_C. \quad (\text{B4})$$

Computing the last four terms of Eq. (B4), we find that the first two terms are more than one order of magnitude larger than the last two terms. The last two terms are henceforth neglected, which leaves

$$\delta(B \overline{v'T'}) \cong \delta B (\overline{v'T'})_C + \delta(\overline{v'T'}) B_C. \quad (\text{B5})$$

Similarly, eddy heat flux $\overline{v'T'}$ may be decomposed. Mathematically, eddy heat flux is a covariance, and therefore

$$\overline{v'T'} = s_v s_T r. \quad (\text{B6})$$

Here s_v and s_T are the longitudinal sample standard deviations of v and T , respectively, while r is the longitudinal correlation between v and T . Decomposing Eq. (B6) into climatological and anomalous components yields

$$(\overline{v'T'})_C + \delta(\overline{v'T'}) = [(s_v)_C + \delta s_v][(s_T)_C + \delta s_T](r_C + \delta r). \quad (\text{B7})$$

After multiplying through the right-hand side, Eq. (B7) becomes

$$\begin{aligned} (\overline{v'T'})_C + \delta(\overline{v'T'}) &= (s_v)_C (s_T)_C r_C + \delta s_v (s_T)_C r_C + \delta s_T (s_v)_C r_C + \delta r (s_v)_C (s_T)_C \\ &\quad + \delta s_v \delta s_T r_C + \delta s_v \delta r (s_T)_C + \delta s_T \delta r (s_v)_C + \delta s_v \delta s_T \delta r. \end{aligned} \quad (\text{B8})$$

Taking the climatological mean of Eq. (B8) produces the following two equations:

$$\begin{aligned} (\overline{v'T'})_C &= (s_v)_C (s_T)_C r_C + (\delta s_v \delta s_T r_C)_C + [\delta s_v \delta r (s_T)_C]_C \\ &\quad + [\delta s_T \delta r (s_v)_C]_C + (\delta s_v \delta s_T \delta r)_C \quad \text{and} \end{aligned} \quad (\text{B9})$$

$$\begin{aligned} \delta(\overline{v'T'}) = & \delta s_v(s_T)_C r_C + \delta s_T(s_v)_C r_C + \delta r(s_v)_C (s_T)_C + \delta s_v \delta s_T r_C + \delta s_v \delta r (s_T)_C + \delta s_T \delta r (s_v)_C + \delta s_v \delta s_T \delta r \\ & - (\delta s_v \delta s_T r_C)_C - [\delta s_v \delta r (s_T)_C]_C - [\delta s_T \delta r (s_v)_C]_C - (\delta s_v \delta s_T \delta r)_C. \end{aligned} \quad (\text{B10})$$

The last eight terms of Eq. (B10) may be neglected because they are calculated to be at least an order of magnitude smaller than the first three terms. Therefore, anomalous meridional eddy heat flux may be formulated as

$$\begin{aligned} \delta(\overline{v'T'}) \cong & \delta s_v(s_T)_C r_C + \delta s_T(s_v)_C r_C \\ & + \delta r(s_v)_C (s_T)_C. \end{aligned} \quad (\text{B11})$$

Substituting Eq. (B11) into Eq. (B5) gives

$$\begin{aligned} \delta(B\overline{v'T'}) \cong & \delta B(\overline{v'T'})_C + \delta s_v(s_T)_C r_C B_C + \delta s_T(s_v)_C r_C B_C \\ & + \delta r(s_v)_C (s_T)_C B_C. \end{aligned} \quad (\text{B12})$$

Thus, anomalous baroclinic conversion per unit mass may be approximated by the sum of the four terms on the right-hand side of Eq. (B12), where each of the four terms contains one anomalous variable: δB , δs_v , δs_T , and δr .

REFERENCES

- Brown, D., R. Brownrigg, M. Haley, and W. Huang, 2013: NCAR command language version 6.1.2. UCAR/NCAR Computational and Information Systems Laboratory, doi:10.5065/D6WD3XH5.
- Dee, D. P., and Coauthors, 2011: The ERA-Interim reanalysis: Configuration and performance of the data assimilation system. *Quart. J. Roy. Meteor. Soc.*, **137**, 553–597, doi:10.1002/qj.828.
- Feldstein, S. B., and I. M. Held, 1989: Barotropic decay of baroclinic waves in a two-layer beta-plane model. *J. Atmos. Sci.*, **46**, 3416–3430, doi:10.1175/1520-0469(1989)046<3416:BDOWBI>2.0.CO;2.
- Holton, J. R., 1965: The influence of viscous boundary layers on transient motions in a stratified rotating fluid. Part I. *J. Atmos. Sci.*, **22**, 402–411, doi:10.1175/1520-0469(1965)022<0402:TIOVBL>2.0.CO;2.
- Hoskins, B. J., M. E. McIntyre, and A. W. Robertson, 1985: On the use and significance of isentropic potential vorticity maps. *Quart. J. Roy. Meteor. Soc.*, **111**, 877–946, doi:10.1002/qj.49711147002.
- James, I. N., 1987: Suppression of baroclinic instability in horizontally sheared flows. *J. Atmos. Sci.*, **44**, 3710–3720, doi:10.1175/1520-0469(1987)044<3710:SOBIH>2.0.CO;2.
- , and L. J. Gray, 1986: Concerning the effect of surface drag on the circulation of a baroclinic planetary atmosphere. *Quart. J. Roy. Meteor. Soc.*, **112**, 1231–1250, doi:10.1002/qj.49711247417.
- Karoly, D. J., and B. J. Hoskins, 1982: Three dimensional propagation of planetary waves. *J. Meteor. Soc. Japan*, **60**, 109–123.
- Kim, H.-K., and S. Lee, 2004: The wave–zonal mean flow interaction in the Southern Hemisphere. *J. Atmos. Sci.*, **61**, 1055–1067, doi:10.1175/1520-0469(2004)061<1055:TWMFII>2.0.CO;2.
- Köhler, M., M. Ahlgrimm, and A. Beljaars, 2011: Unified treatment of dry convective stratocumulus-topped boundary layers in the ECMWF model. *Quart. J. Roy. Meteor. Soc.*, **137**, 43–57, doi:10.1002/qj.713.
- Lachmy, O., and N. Harnik, 2009: A wave amplitude transition in a quasi-linear model with radiative forcing and surface drag. *J. Atmos. Sci.*, **66**, 3479–3490, doi:10.1175/2009JAS3157.1.
- Lee, S., 2010a: Finite-amplitude equilibration of baroclinic waves on a jet. *J. Atmos. Sci.*, **67**, 434–451, doi:10.1175/2009JAS3201.1.
- , 2010b: Dissipative energization of baroclinic waves by surface Ekman pumping. *J. Atmos. Sci.*, **67**, 2251–2259, doi:10.1175/2010JAS3295.1.
- , and I. M. Held, 1991: Subcritical instability and hysteresis in a two-layer model. *J. Atmos. Sci.*, **48**, 1071–1077, doi:10.1175/1520-0469(1991)048<1071:SIAHIA>2.0.CO;2.
- Li, L., A. P. Ingersoll, X. Jiang, D. Feldman, and Y. L. Yung, 2007: Lorenz energy cycle of the global atmosphere based on reanalysis datasets. *Geophys. Res. Lett.*, **34**, L16813, doi:10.1029/2007GL029985.
- Lorenz, E. N., 1955: Available potential energy and the maintenance of the general circulation. *Tellus*, **7**, 157–167, doi:10.1111/j.2153-3490.1955.tb01148.x.
- Mason, P. J., and R. I. Sykes, 1978: On the interaction of topography and Ekman boundary layer pumping in a stratified atmosphere. *Quart. J. Roy. Meteor. Soc.*, **104**, 475–490, doi:10.1002/qj.49710444018.
- Matsumo, T., 1970: Vertical propagation of stationary planetary waves in the winter Northern Hemisphere. *J. Atmos. Sci.*, **27**, 871–883, doi:10.1175/1520-0469(1970)027<0871:VPOSPW>2.0.CO;2.
- Moon, W., and S. B. Feldstein, 2009: Two types of baroclinic life cycles during the Southern Hemisphere summer. *J. Atmos. Sci.*, **66**, 1401–1417, doi:10.1175/2008JAS2826.1.
- Oort, A. H., 1983: *Global Atmospheric Circulation Statistics, 1958–1973*. U.S. Government Printing Office, 180 pp.
- Palmer, T. N., 1982: Properties of the Eliassen–Palm flux for planetary-scale motions. *J. Atmos. Sci.*, **39**, 992–997.
- Peixoto, J. P., and A. H. Oort, 1974: The annual distribution of atmospheric energy on a planetary scale. *J. Geophys. Res.*, **79**, 2149–2159, doi:10.1029/JC079i015p02149.
- Randel, W. J., and J. L. Stanford, 1985: The observed life cycle of a baroclinic instability. *J. Atmos. Sci.*, **42**, 1364–1373, doi:10.1175/1520-0469(1985)042<1364:TOLCOA>2.0.CO;2.
- Rivière, G., and A. Joly, 2006: Role of the low-frequency field on the explosive growth of extratropical cyclones at the jet exit. Part II: Baroclinic critical region. *J. Atmos. Sci.*, **63**, 1982–1995, doi:10.1175/JAS3729.1.
- Simmons, A. J., and B. J. Hoskins, 1978: The life cycles of some nonlinear baroclinic waves. *J. Atmos. Sci.*, **35**, 414–432, doi:10.1175/1520-0469(1978)035<0414:TLCOSN>2.0.CO;2.
- , and —, 1980: Barotropic influences on the growth and decay of nonlinear baroclinic waves. *J. Atmos. Sci.*, **37**, 1679–1684, doi:10.1175/1520-0469(1980)037<1679:BIOTGA>2.0.CO;2.